Intrinsic and extrinsic plasmons in the hard x-ray photoelectron spectra of nearly free electron metals

Mohammad Balal [1], Shuvam Sarkar [1], Pramod Bhakuni [1], Andrei Gloskovskii [2]
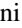Aparna Chakrabarti [3,4] and Sudipta Roy Barman [1,*]

[1]*UGC-DAE Consortium for Scientific Research, Khandwa Road, Indore 452001, Madhya Pradesh, India*
[2]*Deutsches Elektronen-Synchrotron DESY, Notkestrasse 85, D-22607 Hamburg, Germany*
[3]*Raja Ramanna Centre for Advanced Technology, Indore 452013, Madhya Pradesh, India*
[4]*Homi Bhabha National Institute, Training School Complex, Anushakti Nagar, Mumbai 400094, Maharashtra, India*

Collective plasmon excitations in solids that result from the process of photoemission are an important area of fundamental research. In this study, we identify a significant number (n) of multiple bulk plasmons ($n\omega_p$) in the hard x-ray photoelectron spectra of the core levels and valence bands (VBs) of two well-known, nearly free electron metals, aluminum (Al) and magnesium (Mg). On the basis of earlier theoretical works, we estimate the contributions of extrinsic, intrinsic, and interference processes to the intensities of $1s$ to $2s$ core-level plasmons. The intrinsic contribution diminishes from 21.7% for $1\omega_p$ to 4.4% for $2\omega_p$, and becomes negligible thereafter (0.5% for $3\omega_p$). The extrinsic and intrinsic plasmon contributions do not vary significantly across a broad range of photoelectron kinetic energies, and also between the two metals (Al and Mg). The interference contribution varies from negative to zero as n increases. An asymmetric line shape is observed for the bulk plasmons, which is most pronounced for $1\omega_p$. Signature of the surface plasmon is detected in normal emission, and it exhibits a significantly increased intensity in the grazing emission. The VB spectra of Al and Mg, which are dominated by s-like states, exhibit excellent agreement with the calculated VB based on density functional theory. The VB exhibits four multiple bulk plasmon peaks in the loss region, which are influenced by an intrinsic process in addition to the extrinsic process. On a completely oxidized aluminum surface, the relative intensity of the Al metal bulk plasmon remains nearly unaltered, while the surface plasmon is completely attenuated.

I. INTRODUCTION

The investigation of plasmon excitations in photoelectron spectra of free electron metals has been a central focus of fundamental research for over four decades, with ongoing theoretical [1–22] and experimental [23–37] investigations. These investigations have provided valuable insights into the physics of plasmons in the nearly free electron metals. Furthermore, continuous interest in this field highlights its relevance and potential for further advancements in our understanding of collective electronic excitations and the development of various future applications, such as plasmonics. The bulk and surface plasmons, observed as loss features in the core-level photoelectron spectra, are dominated by an extrinsic process that results from the Coulomb interaction of the conduction electrons with the photoelectron traversing through the solid from the photoemission site to the surface. An additional contribution to the plasmon intensity comes from an intrinsic process, where the sudden change in the potential due to the formation of a localized core hole attracts the conduction electrons to screen it, resulting in a plasmon oscillation. From the variation of successive multiple bulk plasmon ($n\omega_p$) intensity in Al $2s$ x-ray photoemission spectroscopy (XPS), the intrinsic plasmon was estimated to be 14%–25% of the total intensity [30,33]. Furthermore, an

interference [11–13,22,25,30] between the intrinsic and extrinsic processes, where virtual plasmons created by one are absorbed by the other, plays an important role in determining the shape of the plasmons. Hedin [8] pointed out that the interference term should decrease as a function of the photoelectron kinetic energy. The coupling of the Al surface plasmon to the oxygen adsorbed on its surface was observed in the O $1s$ core-level spectra in XPS [35]. Biswas *et al.* [25] determined the relative contributions of the intrinsic, extrinsic, and interference processes in the surface plasmon from the XPS core-level spectra of Al metal. The loss region has been studied for Al and carbon by XPS to identify both the one-electron interband transitions and plasmon excitations [23,26]. Bulk plasmons have been observed in the XPS valence band (VB) spectra of Al [30] and Mg up to $n = 2$–3 [31,34], but their intensities were affected by presence of KLV Auger electron spectroscopy signal and x-ray satellites. The mechanism of instrinsic plasmon production for the VB, where, unlike the core level, the photohole is delocalized, was related to many-body effects and electron-electron interaction by theory [13,14].

Hard x-ray photoelectron spectroscopy (HAXPES) has become a vital method to study the bulk electronic structure of materials because of its large inelastic mean-free path (8–10 nm) [38–51]. Previous research has investigated this phenomenon for a limited number of elements, including carbon [52], silicon [53], germanium [54], phosphorous [55], and Al films grown on Si [56]. However, the investigation of

*barmansr@gmail.com

plasmon excitation in nearly free electron metals remains a captivating subject due to the substantial theoretical research that has been undertaken in this area previously [1,3–22,57]. Notwithstanding this, theoretical investigations of plasmons in free electron metals in the HAXPES regime are scarce. Shinotsuka *et al.* [3] performed a full quantum mechanical calculation, taking the interference term into account, using the model suggested by Hedin *et al.* [10]. Fujikawa *et al.* have attempted to address this issue through the application of the quantum Landau formula, which accounts for elastic scatterings both prior to and subsequent to the loss [4]. These works show that in the HAXPES regime, the extrinsic contribution is dominant, although both the positive intrinsic and the negative interference terms are present. The interference and intrinsic contributions decrease very slowly as a function of the photoelectron energy and are therefore significant even at a large photon energy of 10 keV. Even the surface plasmon exhibits a peak of significant intensity at this photon energy [4]. The other interesting theoretical result [3] is that the loss features hardly exhibit any angular dependence, i.e., the grazing versus the normal emission spectra are nearly similar. This behavior is different compared to the low photon energy XPS regime [3,7,11,12,25]. The above-discussed intriguing characteristics of the plasmons, as postulated by theory [3,4], have yet to be empirically investigated.

HAXPES study of the core-level and VB plasmons in free electron metals is scarce in previous literature, despite the fact that this technique offers unique advantages over XPS due to its deeper probing depths. Another benefit of HAXPES over XPS is that the former does not experience interference from the Auger electron spectroscopy signal. A recent study on Al thin films on Si and that of fractured Al metal reported Al $1s$ related plasmons [56]. However, the Si(111) surface was naturally oxidized and the *ex situ* introduced Al films were inhomogeneous and showed a large Al-oxide component in the Al $1s$ spectrum. Thus, although bulk plasmons for clean bulk Al were observed, the thin-film related Al plasmons were affected by presence of oxide and Si related loss features.

Here, we present a detailed HAXPES study of the plasmon excitations in the VB and core-level spectra for clean Al and Mg bulk single crystals. A large number of multiple bulk plasmons ($n\omega_p$) up to $n = 13$ are observed, in addition to a relatively weaker surface plasmon (ω_s). We conduct exhaustive multiparameter curve fitting considering the plasmons to ascertain the variation of their intensity and shape. From the intensity variation, the intrinsic, extrinsic, and interference contributions to $n\omega_p$ are determined based on prior theoretical works [14,19,21,22,57]. Normal and grazing emission properties of the bulk and surface plasmons have been investigated and compared with an oxidized Al surface. In addition, our work shows the existence of the intrinsic process in the VB -related bulk plasmons.

II. METHODS

The experiments were carried out at the P22 beamline in PETRA III, Deutsches Elektronen-Synchrotron, Hamburg, Germany. A post-monochromator was used to improve the resolution and stability of the photon beam. All the spectra were measured using 6-keV photon energy. The electron

energy analyzer has an angular acceptance angle of $\pm 15°$. The overall energy resolution, including the source and the analyzer contribution, was set at 0.3–0.4 eV, as measured from the Au Fermi edge that was in electrical contact with the specimens. The details of the beam line and the end station can be found in Ref. [58]. The measurements were carried out at $\theta = 85°$ (referred henceforth as normal emission) and $10°$ (grazing emission), where θ is the angle between the analyzer axis and sample surface.

Polished and oriented Al single crystals were cleaned *in situ* by sputtering with Ar^+ ions of energy 3–5 keV for the core-level studies. In the case of the VB and some core-level studies, the Al and Mg crystals were mechanically scraped *in situ* with a diamond file. The binding energy (E) scale of both the core level and valence band spectra has been defined from the Fermi level position of Al/Mg metal (rather than from Au) because of the recoil shift [40,46]; this is discussed later in Sec. III C. The HAXPES core-level main peaks have been fitted using the least-squares error method, where the Doniach-Šunjić (DS) line shape represents the main peak [59]. Asymmetric Lorentzian line shapes have been used to represent the plasmon loss peaks [25,30], as also suggested by the theoretical $1\omega_p$ and $1\omega_s$ line shapes from Ref. [3] shown in Fig. S1 of the Supplemental Material (SM) [60]. The lifetime broadening of the core-level main peak, the DS asymmetry parameter, intensities, peak positions, and the inelastic background have been varied. The half-width at half-maximum of the lifetime broadening and the DS asymmetry parameter for Al (Mg) $2s$, determined from our fitting, are 0.4 (0.32) eV and 0.1 (0.12), respectively. Each of the plasmon peaks has been simulated by four parameters: intensity, position, and an asymmetric Lorentzian [61] with independently varying left (Γ_L) and right (Γ_R) half-width at half-maximum. Aside from the $n\omega_p$ peaks, $2\omega_s$, $1\omega_p+1\omega_s$, and $2\omega_p+1\omega_s$ surface plasmons were also considered for Al $1s$. The inelastic background was simulated by the Tougaard method [62,63] (for Al 1s, a polynomial function was also added for $E > 1660$ eV), whereas use of the Shirley method resulted in an unphysically large value of the intrinsic plasmon probability. As in our earlier works [25,64], all the parameters were not varied simultaneously to avoid unphysical solutions: for example, the parameters for plasmons with $n \geqslant 7$ were varied individually. Thus, the number of independently variable parameters for 1s (2s) was 68 (39).

The calculation of the electronic properties of the bulk Al and Mg metals has been performed using the all-electron full potential linear augmented plane-wave (FPLAPW) method, including scalar relativistic corrections, by employing the density functional theory (DFT) based WIEN2K [65] program package. For the exchange-correlation functional, we consider the generalized gradient approximation over the local density approximation, given by Perdew, Burke, and Ernzerhof (PBE) [66]. Energy cutoff values of about 15 Ry have been used in the calculations. The charge density cutoff is 14. Further, we have used 10 as the maximum value of angular momentum for the (l, m) expansion of wave function and density. The convergence criteria for energy and charge have been taken to be 10^{-5} Ry and 0.001 e^{-1}, respectively. The total density of states (DOS) is calculated from the Kohn-Sham orbitals, and its integration up to the Fermi level gives the total number

of valence electrons. The partial DOS (PDOS) is obtained by projecting the total DOS for each orbital (s, p, d). For Al and Mg with delocalized states, touching muffin-tin sphere was taken to minimize the discrepancy between the total DOS and the sum of all the PDOS.

To calculate the theoretical VB, the angular momentum projected PDOS was multiplied by the corresponding photoemission cross sections per electron calculated for 6-keV photon energy by Trzhaskovskaya *et al.* [67]. In the case where an energy level is not occupied and so the cross section is not calculated, the closest value is assumed, as in our previous work [50,68]. For example, for Mg p PDOS, the cross section is taken to be the same as that of Al p. Furthermore, the partial contributions are added and multiplied by the Fermi function and subsequently convoluted with a Gaussian function representing the instrumental resolution. Additionally, an energy-dependent Lorentzian broadening given by $\mu \times E$ has been used, where E is the binding energy and μ is taken to be 0.15 eV [69,70].

III. RESULTS AND DISCUSSION

A. Multiple bulk plasmons in aluminum core-level spectra

<u>Al 1s</u>. The Al 1s core-level spectrum in Fig. 1(a) shows multiple bulk plasmon peaks ($n\omega_p$) with n as large as 13, as is evident from the magnified spectrum. These plasmons appear on the higher binding energy (E) side, i.e., the loss region of the main peak at 1559.3 eV. The first bulk plasmon peak ($1\omega_p$) appears at ω_p loss energy, and the subsequent $n\omega_p$ multiple plasmons appear at equal ω_p intervals. The positions of the plasmon peaks thus provide an average estimate of ω_p to be 15.3 eV; a similar value is obtained from Al 2s plasmons in Fig. 2(a). The reasons that a large number of multiple bulk plasmons could be observed are large photoemission cross section of the s states at high photon energy (6 keV), the large flux of the photon beam, the $n = 7$–13 plasmon region recorded with larger dwell time, and the absence of any other photoelectron or Auger peaks that could obfuscate the plasmons. The $1\omega_s$ surface plasmon is also distinctly visible, as shown by the blue arrow. The behavior of this surface plasmon will be discussed further in Sec. III B. Bulk plasmons up to $n = 7$ and the $1\omega_s$ surface plasmon in the 1s spectrum of Al metal were reported recently [56], but quantitative analysis of their shapes and intensities was not performed.

Here, based on rigorous multiparameter curve fitting, the normalized intensities [$b(n)$, i.e., area under $n\omega_p$ divided by that of the main peak] and shapes [left (Γ_L) and right (Γ_R) half-width at half-maximum of an asymmetric Lorentzian [61]] have been determined. Aside from taking a realistic shape of the bulk plasmons justified by theory in Sec. III B, inclusion of weak surface plasmon contributions such as $2\omega_s$ (red arrow), $1\omega_p + 1\omega_s$ (black tick), and $2\omega_p + 1\omega_s$ (red tick), improves the quality of the fitting. We find that $b(n)$ determined from the area of the plasmons obtained from fitting (shaded with different colors) decreases with n, as shown by the red open circles in Fig. 1(b). This variation can be explained by Eq. (1), as discussed later. Figure 1(c) portrays the asymmetric shape of $n\omega_p$, where Γ_R is smaller compared to Γ_L. Both show a nearly similar increasing trend with n.

The larger width of $(n + 1)\omega_p$ compared to $n\omega_p$ is because the former is excited by the latter and can be regarded as the self-convolution of the latter [37]. The asymmetry can be quantified by the ratio $\Gamma_L/\Gamma_R (= \kappa)$, its variation with n is shown in Fig. 1(d).

<u>Al 2s</u>. Figure 2(a) shows the Al 2s spectrum at normal emission, showing multiple plasmon peaks $n\omega_p$ up to $n = 7$ (compared to $n = 13$ for Al 1s) because of the relatively lesser photoemission cross section of 2s compared to 1s. The intensity of the former is $\sim$9 times less, as shown by the Al survey spectrum in Fig. S2 of SM [60]. For the same reason, although $1\omega_s$ surface plasmon is also distinctly visible at 10.4 eV loss energy (blue arrow), the multiple surface plasmons are not apparent. Another reason for smaller n is that Ar 2p and 2s peaks at $E = 242.2$ and 320.3 eV, respectively (Fig. S2 of SM [60]) interfere because a small amount of Ar is implanted during the sputtering process [71,72]. In particular, the Ar 2p peak coincides with the eighth plasmon, and the former has a larger intensity. Additionally, the Al related plasmons excited by the Ar 2p photoelectrons [73] overlap with $n > 7$ plasmons. $b(n)$ determined from multiparameter curve fitting is shown in Fig. 2(b). Figure 2(c) shows that the asymmetry of the Al 2s plasmons is qualitatively similar to that of the Al 1s: Γ_R is smaller than Γ_L, and both increase with n. The asymmetry in the plasmon line shape given by κ decreases from about 2.7 ($n = 1$) to about 1.8 for $n \geqslant$ 2–3 [Fig. 2(d)].

Bulk plasmon intensity variation. The decrease of $b(n)$ with n has been studied theoretically by different groups [19,21,22,57] to ascertain the contributions of the different processes connected to the bulk plasmon. Based on perturbation theory arguments, considering only the extrinsic process, it was suggested that $b(n)$ should vary as α^n, where α is a measure of the extrinsic plasmon probability [19,21,22,57]. But the black dashed curve that is obtained using this expression shows a large systematic deviation, as shown by the residual in the top panel of Fig. 1(b) in same line type. This shows that, in addition to the extrinsic process, the intrinsic and interference processes could also be significant. So, a modified Langreth equation [21,22,25,57] that considers all three terms has been used to represent $b(n)$ as follows:

$$b(n) = \alpha^n \sum_{m=0}^{n} \frac{[(\beta - c\chi)/\alpha]^m}{m!}, \quad (1)$$

where β is the measure of the probability of the intrinsic process for the nth plasmon [74]. χ is the probability of the interference process [21,57] given by the product of intrinsic and extrinsic plasmon probabilities [75], where c is the proportionality constant [25]. If the above expression is used to fit the experimental $b(n)$ by varying α, β, and c, the quality of the fitting (blue curve) improves substantially, which is evident from a reduction in χ^2 error by a factor of about 2.5 and comparison of the residuals (blue solid and black dashed lines) in the top panel. From the fitting, we obtain $\alpha = 0.54 \pm 0.05$ and $\beta = 0.19 \pm 0.1$. The experimental value of α is in good agreement with the theoretically suggested value of 0.5 by Chang and Langreth [21,57]. The interference term (black dotted-dashed curve) is found to be finite but negative, with a rapidly decreasing contribution that becomes nearly zero for $n > 3$.
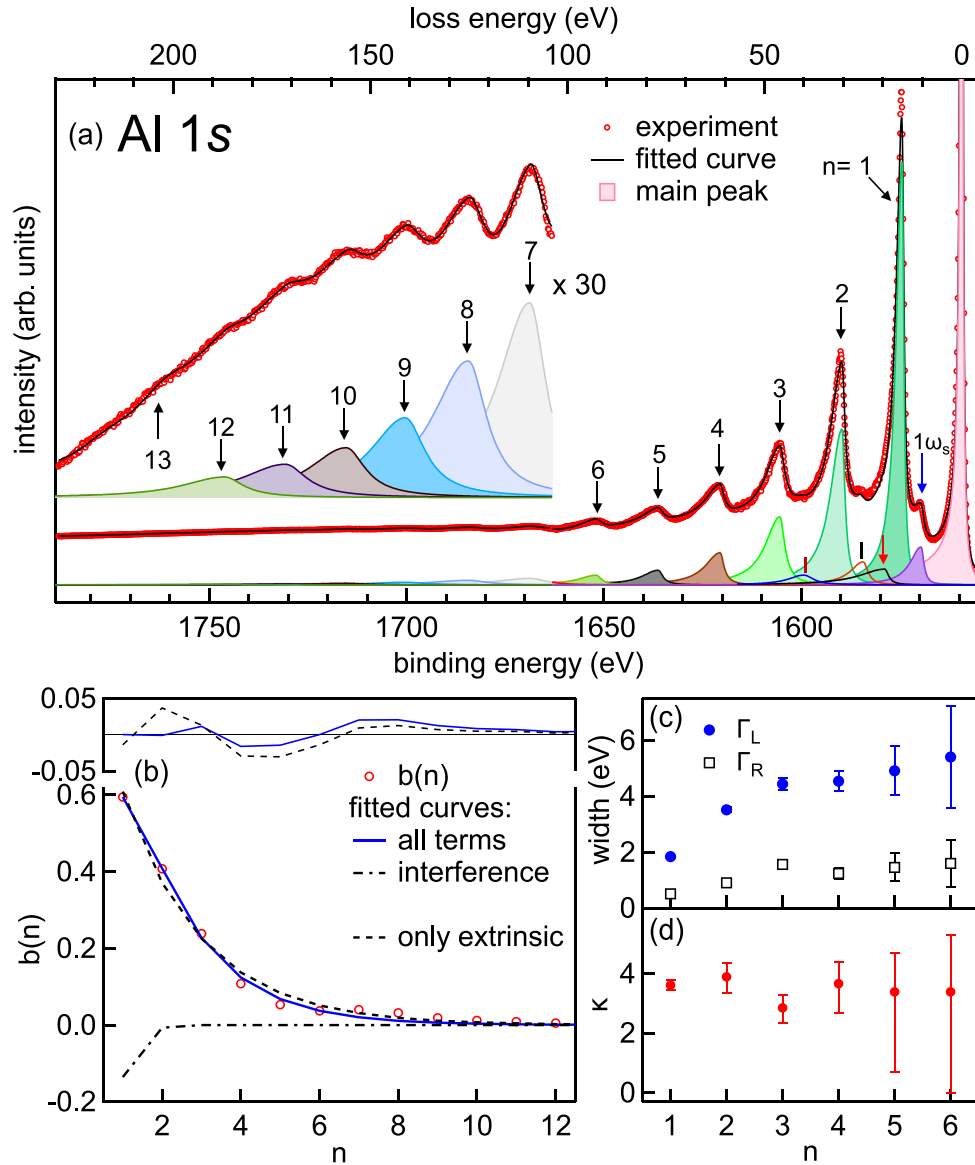
FIG. 1. (a) Al 1*s* core-level spectrum (red open circles) of Al metal taken at normal emission ($\theta = 85°$) showing multiple bulk plasmon peaks $n\omega_p$ ($n = 1$–13, black arrows). The blue (red) arrow shows the $1\omega_s$ ($2\omega_s$) surface plasmon. Black (red) tick represents the $1\omega_p + 1\omega_s$ ($2\omega_p + 1\omega_s$) plasmon. The loss energy scale (the top horizontal axis) is defined with respect to the main peak. The latter is truncated to show the plasmon peaks on an expanded scale. The spectrum for $n = 7$ to 13 is shown separately in a magnified scale. The fitted curve (black) and each of the $n\omega_p$ peaks are shown. (b) The normalized intensity of the bulk plasmons [$b(n)$] fitted with Eq. (1) that includes all the terms, i.e., extrinsic, intrinsic, and interference (blue curve) and with only the extrinsic term (black dashed curve). The corresponding residuals of the fitting are shown in the top panel in same line type. (c) Γ_R, Γ_L, and (d) κ ($= \Gamma_L/\Gamma_R$) as a function of n.

$b(n)$ for Al 2*s* has been fitted using Eq. (1), as shown by the blue curve in Fig. 2(b). The residual in the upper panel demonstrates the good quality of the fitting. On the other hand, the fit is worse if only the extrinsic term is considered. From the fitting, we find that $\alpha = 0.53 \pm 0.05$ and $\beta = 0.18 \pm 0.1$. Thus, the extrinsic and intrinsic contributions are similar between 2*s* and 1*s*, although for the former, the kinetic energy (E_k) of the electrons is larger (5831 eV) compared to the latter (4390 eV). Al 2*s* recorded by XPS, where E_k is relatively smaller (1133 eV), gave α ($= 0.46$ eV) and β ($= 0.22$ eV) [25] that are not significantly different from the HAXPES values. This shows that, contrary to the expectation that the

extrinsic process might be dominant at larger E_k due to larger inelastic mean-free path of the photoelectrons, all three processes have nearly similar contributions over a large range of E_k from 1133 eV (≈ 1 keV) to 5831 eV (≈ 6 keV). This is in agreement with the theoretical study by Shinotsuka *et al.* [3] that shows hardly any change in the different processes in the $1\omega_p$ bulk plasmon of Al in the $h\nu$ range of 2 to 5 keV.

The interference term (black dotted-dashed curve) also shows a similar trend. Its contribution at $n = 1$ is also nearly similar: -0.14 ± 0.05 for 1*s* and -0.17 ± 0.05 for 2*s* using HAXPES, while it is reported to be -0.2 for 2*s* from XPS [25]. This is in agreement with the calculation by Shinot-
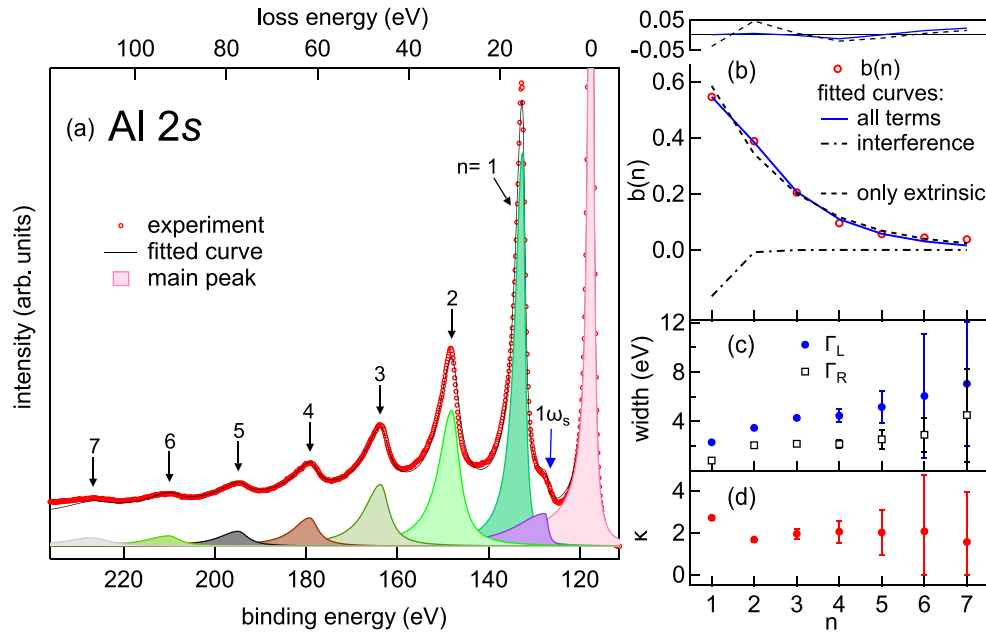
FIG. 2. (a) Al 2s core-level spectrum of Al metal taken at normal emission showing multiple bulk plasmon peaks $n\omega_p$ ($n = 1$–7, black arrows) and a surface plasmon peak ($1\omega_s$, blue arrow). The black curve through the data points (red open circles) and each of the $n\omega_p$ peaks (shaded by different colors) are obtained from the least-squares curve fitting. (b) $b(n)$ fitted with Eq. (1) (blue curve) and with only the extrinsic term (black dashed curve), the respective residuals of the fitting are shown in the top panel. (c) Γ_L, Γ_R, and (d) κ ($= \Gamma_L/\Gamma_R$) as function of n.

suka *et al.* [3], who found that the interference term does not decrease in the HAXPES regime, which however is in disagreement with the prediction by Hedin [8].

B. Multiple bulk plasmons in magnesium core-level spectra

Mg 2s spectrum of clean Mg metal at normal emission, as depicted in Fig. 3(a), also exhibits multiple plasmon peaks denoted by $n\omega_p$ ($n = 1$–7). ω_p of Mg, determined from the average separation of the plasmon peaks from the main peak, is 10.6 eV. It is considerably smaller because of the smaller electron number density of Mg, which has 2 electrons in the outer shell compared to 3 electrons in Al. A weak surface plasmon is observed at 7.5-eV loss energy (blue arrow). Using curve fitting as in case of Al, $b(n)$ for Mg has been determined [Fig. 3(b)]. The residual (blue curve) in the top panel shows good quality of the fitting using Eq. (1). The values of α and β turn out to be 0.55 ± 0.05 and 0.18 ± 0.1, respectively. These values are nearly similar to Al. The interference term for Mg (black dotted-dashed curve), as in the case of Al, is negative for $n = 1$ and decreases to almost zero for $n \geqslant 3$. Figure 3(c) shows that the asymmetry of the Mg 2s plasmons given by κ decreases from about 4 ($n = 1$) to below 2 for $n = 3$ [Fig. 3(d)]. This was also observed for Al 2s. Larger κ, i.e., asymmetry in the $1\omega_p$ plasmon shape compared to $n \geqslant 2$ is because of the sizable intrinsic and interference plasmon contributions that are more asymmetric in shape compared to the extrinsic plasmon [7].

The α and β values obtained for Mg 2s are nearly similar to those from Al 1s and 2s. Thus, the average representative values for these free electron metals are $\alpha = 0.54 \pm 0.05$ and $\beta = 0.18 \pm 0.1$. Considering these values, the ratio of the intrinsic to extrinsic plasmon probabilities [$e^{-\beta}\beta:\alpha$ from

Eq. (11) of Ref. [25]] for $1\omega_p$ turns out to be 0.277:1. For $2\omega_p$ the probability ratio ($e^{-\beta}\beta^2/2! : \alpha^2$) is 0.046:1, whereas for $3\omega_p$ it is 0.005:1 ($e^{-\beta}\beta^3/3! : \alpha^3$). Thus, the intrinsic plasmon contribution decreases rapidly with n from 21.7% ($n = 1$) to 4.4% ($n = 2$), and becomes negligible thereafter (0.5% for $n = 3$).

C. Surface plasmon behavior in the Al 2s core-level spectra

This subsection is dedicated to an in-depth analysis of the surface plasmon. Figures 4(a) and 4(b) show the $1\omega_s$ along with $1\omega_p$ in Al 2s spectra of a polished surface cleaned by Ar ion sputtering. Comparison of the $1\omega_s$ intensity between normal emission in Fig. 4(a) and grazing emission in Fig. 4(b) shows a sizable enhancement in the latter. From the curve fitting, we quantify this by the normalized intensity of $1\omega_s$ i.e., $s(1)$ (the intensity of $1\omega_s$ divided by the main peak). $s(1)$ increases from 0.13 in normal to 0.44 in grazing emission. However, a direct comparison with the XPS spectra (green open circles) from Ref. [25] shows the surface plasmon is weaker in HAXPES for both normal and grazing emission. This is attributed to diminished extrinsic contribution due to larger velocity (v) of the photoelectron [25,35]. From Figs. 4(a) and 4(b), $b(1)$ decreases from 0.6 in normal to 0.43 in grazing emission, which was related to the variation of extrinsic bulk plasmon contribution with emission angle in theory [32]. The intensity ratio R ($= 1\omega_s/1\omega_p$) = 1 is larger in the grazing compared to normal emission (R = 0.2).

The considerable increase of $s(1)$ and R in the grazing emission discussed above is in disagreement with the theoretical results of Shinotsuka *et al.* [3] for HAXPES, where hardly any difference in the calculated $1\omega_p$ and
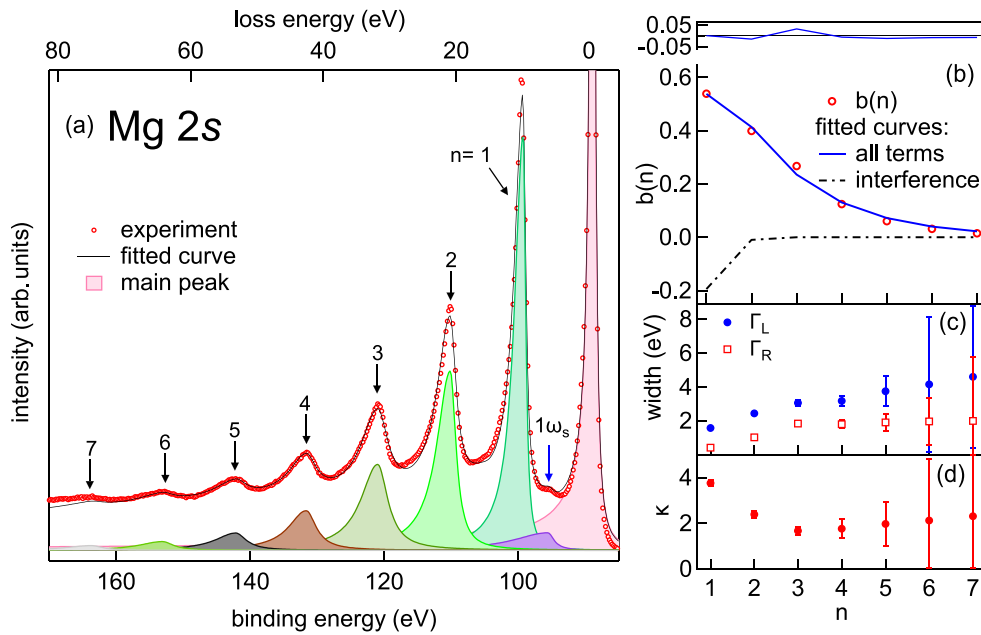
FIG. 3. (a) Mg 2*s* core-level spectrum of Mg metal taken at normal emission showing multiple bulk plasmon peaks $n\omega_p$ ($n = 1$–7, black arrows) and a surface plasmon peak ($1\omega_s$, blue arrow, also shown in the inset). The black curve through the data points (red open circles) and each of the $n\omega_p$ peaks (shaded by different colors) are obtained from the least-squares curve fitting. (b) $b(n)$ fitted with all three terms [extrinsic, intrinsic, and interference, (blue curve)]. The residual of the fitting is shown in the top panel. (c) Γ_L, Γ_R, and (d) κ ($= \Gamma_L/\Gamma_R$) as function of n.

$1\omega_s$ was observed between normal and grazing emission (Fig. S1 of SM [60]). Nevertheless, to obtain an estimate of R from theory, we have fitted the theoretical spectrum using asymmetric Lorentzian shapes for both $1\omega_p$ and $1\omega_s$ from Ref. [3]. A reasonably good fit of the theoretical shape [3] with the asymmetric Lorentzians in Fig. S1 of SM [60] *post priori* justifies the use of the latter to fit the experimental plasmon shapes in Figs. 1–4. From the area under the fitted curves, the theoretical value of R turns out to be close to 0.2, unchanged for both normal and grazing emission. While $R = 0.2$ is in excellent agreement with the experimental normal emission value (0.2), it is conspicuously underestimated for the grazing emission, where the experimental value is 1. Enhancement of $s(1)$ in grazing emission has also been reported for XPS. For example, in Al 2*s* from XPS, a 10 times increase in $s(1)$ has been reported in the grazing emission, which was explained by an increase in v parallel to the surface [25,35]. This effect was possibly not considered in Ref. [3]. Note that in Figs. 4(a) and 4(b), the shape of the surface plasmon is found to be highly asymmetric, with Γ_R considerably smaller than Γ_L. Their ratio κ is 4.9 (7.9) in grazing (normal) emission. The asymmetric shape of the surface plasmon as well as the bulk plasmons is in agreement with Ref. [3] and the earlier theoretical works [11–13].

Figures 4(c) and 4(d) show an interesting result that for rough surface obtained by scraping the polished surface with a diamond file, the enhancement of the surface plasmon in the grazing emission is not as pronounced: $s(1) = 0.14$ in the normal and 0.17 in grazing emission. This is because the emission angle is not well defined for the rough surface. Comparison of Figs. 4(a) and 4(c) shows that both the bulk and surface plasmon intensities in normal emission are, however, nearly

similar between the smooth [$b(1) = 0.6$, $s(1) = 0.14$] and the rough surface [$b(1) = 0.58$, $s(1) = 0.14$].

D. Plasmons in the core-level spectra of a fully oxidized Al surface

In Fig. S3(a) of SM [60], a fully oxidized Al crystal surface shows oxide and metal-related components in the Al 1*s* spectrum. In spite of being fully oxidized, the metal peak is dominant in normal emission compared to the oxide-related peak at 2.7 eV higher E because of the large electron mean-free path in HAXPES (80 Å for Al 1*s* at 6 keV [76]). The thickness of the oxide film estimated from the relative intensity variation of the metal- and the oxide-related peaks with θ [77] turn out to be 48 ± 2 Å. In normal emission, the metal-related bulk plasmon is observed at 15.3-eV loss energy with $b(1) = 0.5$. At the grazing emission in Fig. S3(b) of SM, although the oxide-related peak is highly enhanced in intensity (shown truncated), surprisingly, the $1\omega_p$ corresponding to the metal underneath is still observed with the same ω_p of 15.3 eV and a $b(1)$ value of 0.6. Both these values of $b(1)$ in oxidized Al are close to that of the clean Al metal [$b(1) = 0.6$, Fig. 1(b)]. Thus, the normalized intensity of the bulk plasmon is hardly affected by the oxide layer formed on the surface. This is because both the metal's main peak and the bulk plasmon are similarly attenuated by the oxide layer. However, in contrast, the surface plasmon is completely attenuated because the metal surface is fully covered by the oxide film.

E. Multiple bulk plasmons in the valence band spectra of Al and Mg

The HAXPES valence band (VB) spectrum of Al metal, along with the loss region, shows multiple bulk plasmons $n\omega_p$
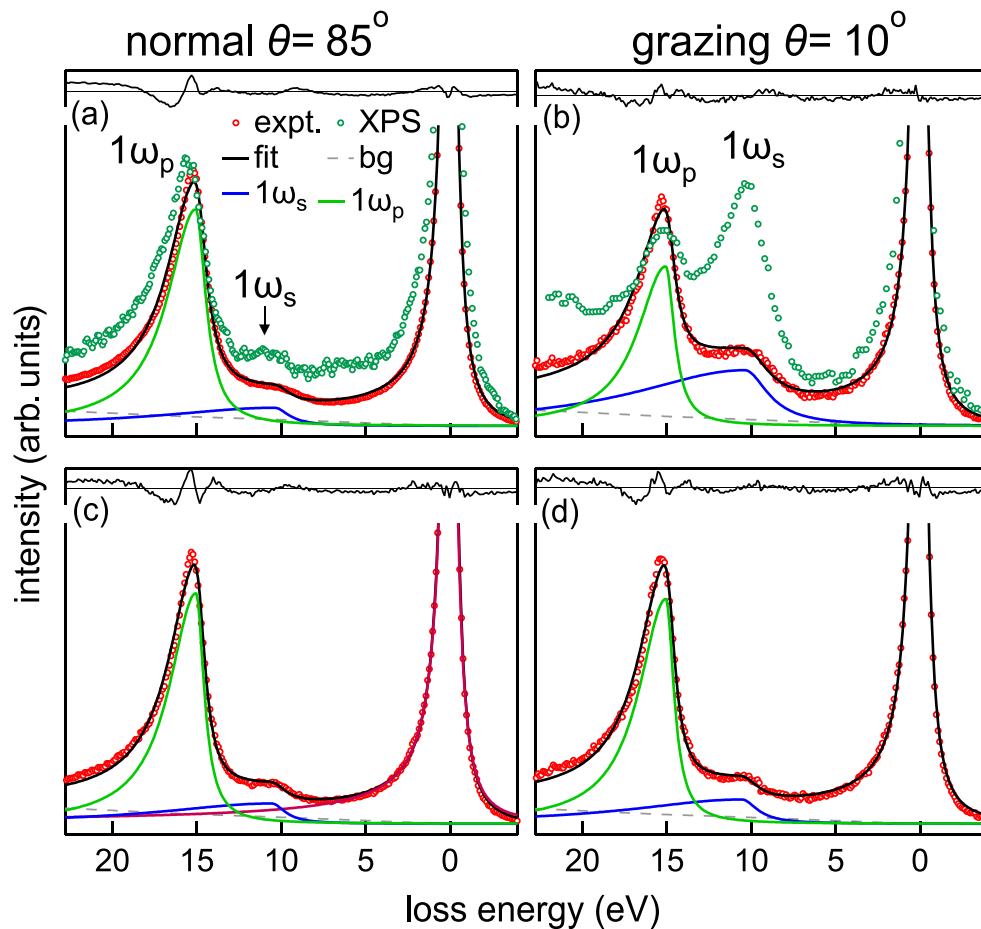
FIG. 4. (a) Normal ($\theta = 85°$) and (b) grazing emission ($\theta = 10°$) Al 2s core-level spectra of Al metal showing the surface plasmon peak ($1\omega_s$) peak along with $1\omega_p$ for a polished smooth surface. XPS data from Ref. [25] are shown for comparison. Al 2s spectra for a scraped rough surface in (c) normal and (d) grazing emission. The fitted curves including the plasmon shapes, the inelastic background (bg), and the residual of fitting (top panel) are shown.

up to $n = 4$ (black arrows) [Fig. 5(a)]. The data were recorded for a scraped surface because, for the sputtered surface, the Ar 3p signal arising from implanted Ar bubbles [71,72] appears at 9.3 eV and interferes with the VB, as shown in Fig. S4 of SM. In Fig. 5(b), the theoretical VB, calculated using the PDOS shown in Fig. 5(c), exhibits excellent agreement with the experiment: All the features, such as a peak near the Fermi level at $E = 1$ eV (blue arrow), a dip at 2 eV (blue tick), a weak feature centered at 3 eV (black arrow), and the broad hump around 6 eV (green arrow), are visible at nearly identical energies and possess similar relative intensities. The VB is largely dominated by the s-like states because of their large photoemission cross section for hard x rays [39,40,51,78]. The small contribution from p-like states is rather featureless. It should be noted that the interstitial (int) contribution to the total DOS is significant because a substantial part of the electron density lies outside the atomic sphere that is used to calculate the PDOS [Fig. 5(c)]. Another point to note is that the PDOS of Al previously calculated using the KKR method [79] differs considerably from our calculation [e.g., compare Fig. 5(c) with the inset of Fig. S5 in SM [60]]. We used the PDOS from Ref. [79] to calculate the VB and find that it differs significantly from the experiment

(Fig. S5 of SM [60]): a peak at ∼5 eV is evident. This is absent in the experimental spectrum, while the dip at ∼2 eV (blue tick) is overestimated. These observations show the shortcomings of the previous calculation, which is possibly related to unphysical fluctuations on the lower-energy side and was performed with constant potential outside the muffin tin sphere [79].

In the case of Mg metal, the VB spectrum also shows multiple bulk plasmons $n\omega_p$ up to $n = 4$ with $\omega_p \sim 10.5$ eV [black arrows in Fig. 5(e)]. The VB, shown on an expanded scale in Fig. 5(f), exhibits excellent agreement with the theoretical VB, which is calculated using the PDOS shown in Fig. 5(g). An earlier augmented plane-wave calculation [80] of the PDOS for Mg agrees well with our calculation. A peak close to the Fermi level at 0.3 eV (blue arrow), a dip at 0.7 eV (blue tick), and a broad hump around 3 eV (green arrow) are visible at similar energies and exhibit comparable relative intensities [Fig. 5(f)]. Here also, as in the case of Al, the VB is largely dominated by the s-like states. The plasmon loss spectra of the VB have been calculated for Mg and Na by Penn [14], which drew on the work by Langreth [81]. Unlike the core-level intrinsic plasmon that is created by a localized core hole in the final state, the photohole in the VB is delo-
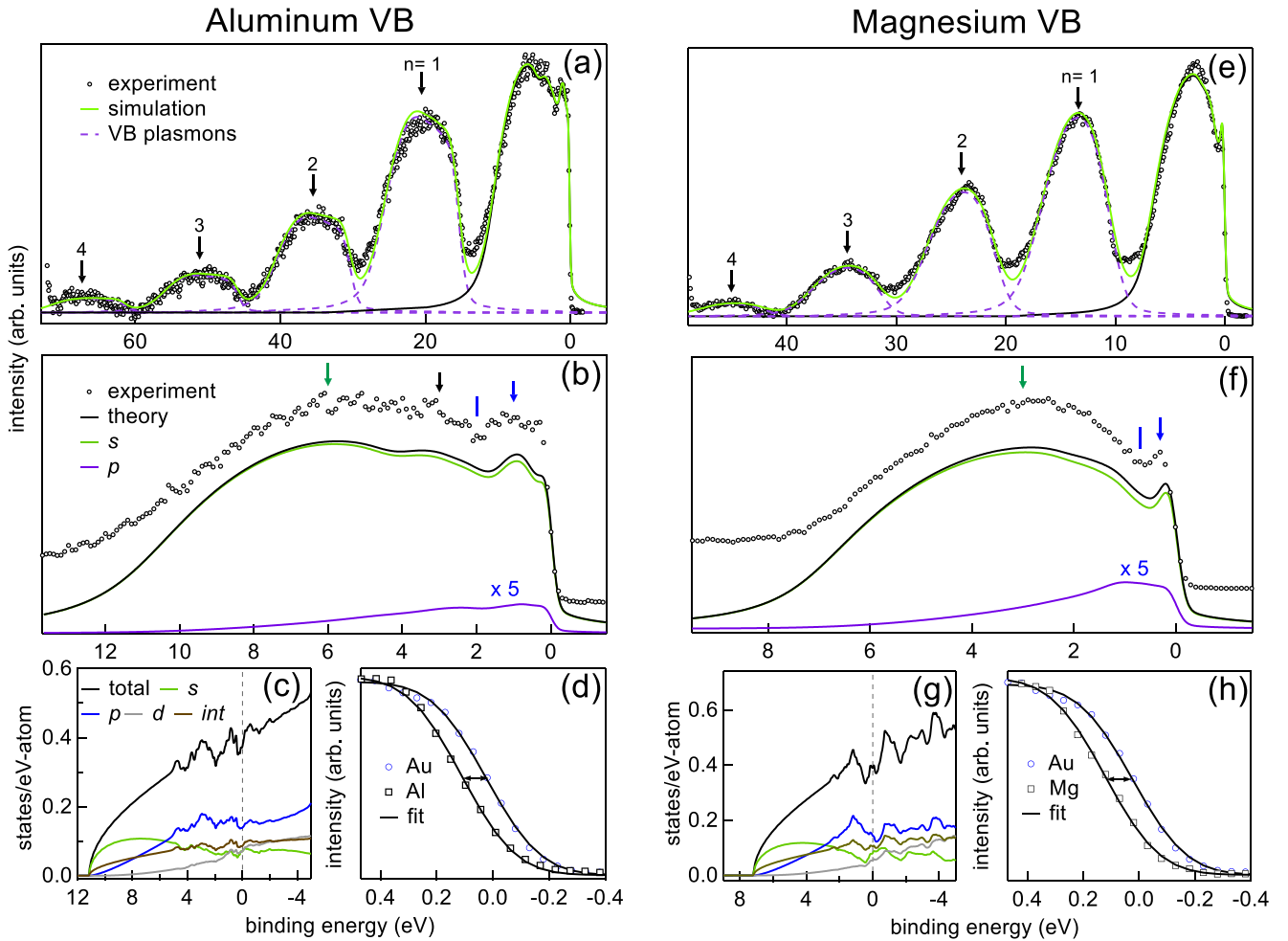
FIG. 5. Inelastic background subtracted HAXPES valence band (VB) of (a) Al and (e) Mg metals along with the bulk plasmon loss peaks ($n\omega_p$ up to $n = 4$ marked by black arrows) measured in normal emission. The simulated plasmon line shapes are shown by violet dashed curves, and their addition is shown by a green curve. (b) Al and (f) Mg VBs are compared with the calculated VB (black curve), the s and p partial contributions are shown. The calculated VBs are shown overlaid in (a) and (e) and are used to simulate the plasmons (see text). The DFT calculated (c) Al and (g) Mg total DOS, s, p, and d PDOS, and the interstitial (int) contribution. The Fermi edges of (d) Al and (h) Mg measured by HAXPES have been compared to Au (black lines are fit to the experimental data); the horizontal double-sided arrow shows the recoil shift.

calized. So, the mechanism of intrinsic plasmon production in the VB was proposed to be related to electron-electron interaction: a second electron creates the intrinsic plasmon via its interaction with the conduction electrons and scatters into the hole left by the photoexcited electron [14]. Although energy dependence and interference effect were not considered in theory [14], remarkable agreement was obtained with the XPS spectra [34] only when both extrinsic and intrinsic plasmons were considered. On the other hand, the plasmon intensities were significantly underestimated if the intrinsic plasmon was not considered. This established the presence of intrinsic plasmons in the XPS VB plasmon in nearly free electron metals [14].

To compare theory and experimental results, the shapes of the nth VB plasmons for both Al and Mg have been simulated by shifting the calculated VB by $n\omega_p$ towards higher E, and allowing the intensity and an additional Gaussian broadening to vary [Figs. 5(a) and 5(e)]. We find that unlike the core-level

plasmons, asymmetric broadening is not required, and the FWHM of the Gaussian remains nearly unchanged with n (2 and 2.5 eV for Al and Mg, respectively). The $b_{\mathrm{VB}}(n)$ values of Mg have also been extracted for the theoretical calculations by Penn [14] for XPS and the XPS spectrum published in the literature [34] (Fig. S6 of SM [60]). This has been done by shifting the calculated XPS VB by $n\omega_p$ and broadening it by a Gaussian, as discussed above. Figure S6 of SM [60] shows good agreement between the calculated and experimental XPS VB. The former is obtained from the PDOS in Figs. 5(c) and 5(g) using the photoemission cross sections for AlK$_\alpha$ (1486.6 eV) radiation [67].

Figure 6 shows $b_{\mathrm{VB}}(n)$, which is the area of the nth plasmon divided by the area of the VB. $b_{\mathrm{VB}}(n)$ for Mg and Al HAXPES VB are close, as shown by the red and blue curves. $b_{\mathrm{VB}}(1)$ for Mg HAXPES (0.87) and XPS (0.9) are quite similar to each other and to the theoretical value (0.9) of Mg that includes the intrinsic and extrinsic plasmons (black filled
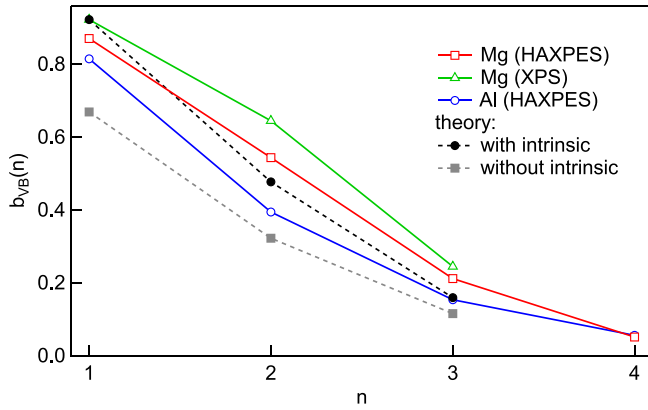
FIG. 6. $b_{\mathrm{VB}}(n)$ as a function of n for Al and Mg HAXPES VB compared with those extracted from Mg XPS VB [34] and the theoretical calculation by Penn [14] for Mg with intrinsic and without intrinsic (i.e., only extrinsic) plasmon contributions.

circle-dashed line). On the other hand, if intrinsic plasmon is not considered, the contribution of only the extrinsic process is significantly less (0.6) (gray filled square-dashed line). Similarly, $b_{\mathrm{VB}}(2)$ and $b_{\mathrm{VB}}(3)$ for both Mg HAXPES and XPS are closer to the theoretical values that include both intrinsic and extrinsic plasmons. Thus, our data provide evidence of the intrinsic plasmon production in the VB-related plasmons of Mg measured by HAXPES.

F. Recoil effect in the valence band spectra of Mg

The recoil effect is well known in the HAXPES core-level spectra of light elements. When a photoelectron of mass m is emitted with a large kinetic energy (E_{kin}) from an atom of mass M, the photoelectron delivers a recoil energy (E_R) to that atom, which is given by $E_R \approx \frac{m}{M} \times E_{\mathrm{kin}}$ [40,46]. The photoelectrons lose this energy, E_R, resulting in a recoil shift towards higher E. This effect has also been observed in the VB of light metals such as Al (atomic mass 27 u) through a shift of the Al metal Fermi edge compared to that of Au [46]. Au, being of high mass (197 u), hardly exhibits this effect. Recently, such a recoil shift in the VB has been reported in a light complex metallic alloy β-Al_3Mg_2 [82]. Here in Fig. 5(d), the recoil shift of Al is, however, smaller (85 meV) compared to 120 meV reported using 7.94 keV [46]. This can be explained by the proportionality of the recoil shift with E_{kin}, i.e., $\frac{6\,\mathrm{keV}}{7.94\,\mathrm{keV}} \times 120\ \mathrm{meV} = 90.7\ \mathrm{meV}$, which is close to 85 meV. Due to marginally smaller mass of Mg (24.3 u) compared to Al, the recoil shift is found to be slightly larger [90 meV, Fig. 5(h)].

IV. CONCLUSION

Multiple bulk plasmons ($n\omega_p$) in the valence band (up to $n = 4$) and core-level spectra (up to $n = 13$) of free electron metals such as Al and Mg have been studied by hard x-ray photoelectron spectroscopy (HAXPES). Based on earlier theoretical works [14,19,21,22,57], estimates of the extrinsic, intrinsic, and interference processes that contribute to the core-level plasmon intensities are obtained from exhaustive multiparameter curve fitting. The probabilities of the extrinsic and intrinsic processes in the core-level plasmons are nearly similar for the two free electron metals, α and β being 0.54 ± 0.05 and 0.18 ± 0.1, respectively. These values imply that, as n increases, the intrinsic plasmon contribution decreases while the interference plasmon changes from negative to zero. Despite the larger inelastic mean-free path in HAXPES, the intrinsic, extrinsic, and interference processes remain nearly unchanged across a broad kinetic energy range (1–6 keV). This finding is consistent with previous theoretical research [3]. The $1\omega_p$ line shape is more asymmetric because of the presence of sizable intrinsic and interference terms. The $1\omega_s$ surface plasmon has been identified in both Al and Mg. Its intensity increases significantly in the grazing emission compared to the normal emission. In the case of oxidized aluminum, the surface plasmon is completely suppressed, while the bulk plasmon intensity is almost unaffected compared to the metal's main peak.

Multiple plasmons are observed in the loss region of the Al and Mg valence bands; the shape of the VB is in excellent agreement with the DFT-based calculated valence band. Comparison with the theoretical calculation [14] after extracting the relative VB plasmon intensities establishes the existence of the intrinsic plasmon, aside from the extrinsic plasmon. The recoil shift observed in both Al and Mg VB is related to the kinetic energy of the photoelectron and the mass of the atom.

[1] A. Mandal, S. Tricot, R. Choubisa, and D. Sébilleau, Model dielectric functions for fluctuation potential calculations in electron gas: A critical assessment, Phys. Rev. B **105**, 195424 (2022).

[2] T. Fujikawa, K. Niki, and M. Haniuda, Intrinsic and extrinsic losses in photoemission spectra, J. Phys. Soc. Jpn. **91**, 064708 (2022).

[3] H. Shinotsuka, T. Uwatoko, T. Konishi, and T. Fujikawa, Theoretical study of plasmon loss peaks in core-level photoemission spectra: Energy and angular dependence, J. Surf. Anal. **14**, 332 (2008).

[4] T. Fujikawa, M. Kazama, and H. Shinotsuka, Theoretical study of plasmon losses in core-level photoemission spectra, e-J. Surf. Sci. Nanotechnol. **6**, 263 (2008).

[5] J. S. Zhou, M. Gatti, J. J. Kas, J. J. Rehr, and L. Reining, Cumulant Green's function calculations of plasmon satellites in bulk sodium: Influence of screening and the crystal environment, Phys. Rev. B **97**, 035137 (2018).

[6] M. Kazama, H. Shinotsuka, Y. Ohori, K. Niki, T. Fujikawa, and L. Kövér, Plasmon losses in core-level photoemission spectra studied by the quantum Landau formula including full multiple scattering, Phys. Rev. B **89**, 045110 (2014).

[7] F. Yubero and S. Tougaard, Quantification of plasmon excitations in core-level photoemission, Phys. Rev. B **71**, 045414 (2005).

[8] W. Schattke and M. A. V. Hove, *Solid-State Photoemission and Related Methods: Theory and Experiment* (Wiley, Hoboken, NJ, 2003), p. 116.

[9] G. D. Mahan, *Many-Particle Physics* (Kluwer Academic, New York, 2000).

[10] L. Hedin, J. Michiels, and J. Inglesfield, Transition from the adiabatic to the sudden limit in core-electron photoemission, Phys. Rev. B **58**, 15565 (1998).

[11] J. E. Inglesfield, Plasmon satellites in core-level photoemission, J. Phys. C: Solid State Phys. **16**, 403 (1983).

[12] J. Inglesfield, Plasmon excitation in core-level photoemission, Solid State Commun. **40**, 467 (1981).

[13] S. M. Bose, S. Prutzer, and P. Longe, Plasmon satellites in the x-ray photoemission spectra of metals and adsorbates, Phys. Rev. B **27**, 5992 (1983).

[14] D. R. Penn, Role of intrinsic plasmons in conduction-band x-ray photoemission from solids, Phys. Rev. Lett. **40**, 568 (1978).

[15] D. R. Penn, Theory of the electron energy-loss spectrum in core-level x-ray photoemission from solids, Phys. Rev. Lett. **38**, 1429 (1977).

[16] Y. Baer and G. Busch, X-ray photoemission from Aluminum, Phys. Rev. Lett. **30**, 280 (1973).

[17] P. H. Citrin, G. K. Wertheim, and Y. Baer, Many-body processes in x-ray photoemission line shapes from Li, Na, Mg, and Al metals, Phys. Rev. B **16**, 4256 (1977).

[18] M. Šunjić and D. Šokčević, Inelastic effects in x-ray photoelectron spectroscopy, J. Electron Spectrosc. Relat. Phenom. **5**, 963 (1974).

[19] D. C. Langreth, *in Collective Properties of Physical Systems: Medicine and Natural Sciences*, edited by B. Lundqvist (Elsevier, Amsterdam, 1974), p. 210.

[20] G. D. Mahan, Electron energy loss during photoemission, Phys. Status Solidi B **55**, 703 (1973).

[21] J.-J. Chang and D. C. Langreth, Deep-hole excitations in solids. I. fast-electron-plasmon effects, Phys. Rev. B **5**, 3512 (1972).

[22] D. C. Langreth, Born-oppenheimer principle in reverse: Electrons, photons, and plasmons in solids—singularities in their spectra, Phys. Rev. Lett. **26**, 1229 (1971).

[23] D. David and C. Godet, Derivation of dielectric function and inelastic mean free path from photoelectron energy-loss spectra of amorphous carbon surfaces, Appl. Surf. Sci. **387**, 1125 (2016).

[24] M. M. Özer, E. J. Moon, A. G. Eguiluz, and H. H. Weitering, Plasmon response of a quantum-confined electron gas probed by core-level photoemission, Phys. Rev. Lett. **106**, 197601 (2011).

[25] C. Biswas, A. K. Shukla, S. Banik, V. K. Ahire, and S. R. Barman, Plasmons in core-level photoemission spectra of Al(111), Phys. Rev. B **67**, 165416 (2003).

[26] V. M. da Silva Santana, D. David, J. S. de Almeida, and C. Godet, Photoelectron energy loss in Al(002) revisited: Retrieval of the single plasmon loss energy distribution by a fourier transform method, Braz. J. Phys. **48**, 215 (2018).

[27] S. R. Barman, C. Biswas, and K. Horn, Electronic excitations on silver surfaces, Phys. Rev. B **69**, 045413 (2004).

[28] S. R. Barman, P. Häberle, K. Horn, J. A. Maytorena, and A. Liebsch, Quantum well behavior without confining barrier observed via dynamically screened photon field, Phys. Rev. Lett. **86**, 5108 (2001).

[29] S. R. Barman, K. Horn, P. Häberle, H. Ishida, and A. Liebsch, Photoinduced plasmon excitations in alkali-metal overlayers, Phys. Rev. B **57**, 6662 (1998).

[30] P. M. Th. M. van Attekum and J. M. Trooster, Bulk- and surface-plasmon-loss intensities in photoelectron, auger, and electron-energy-loss spectra of Al metal, Phys. Rev. B **18**, 3872 (1978).

[31] P. M. Th. M. van Attekum and J. M. Trooster, Bulk- and surface-plasmon-loss intensities in photoelectron, auger, and electron-energy-loss spectra of Mg metal, Phys. Rev. B **20**, 2335 (1979).

[32] R. Baird, C. Fadley, S. Goldberg, P. J. Feibelman, and M. Šunjić, The angular dependence of plasmon loss features in XPS spectra from polycrystalline aluminum: Clean surfaces and effects of oxygen adsorption, Surf. Sci. **72**, 495 (1978).

[33] P. Steiner, H. Höchst, and S. Hüfner, XPS investigation of simple metals: I. core level spectra, Z. Phys. B **30**, 129 (1978).

[34] H. Höchst, P. Steiner, and S. Hüfner, XPS investigation of simple metals: II. the valence band spectra, Z. Phys. B **30**, 145 (1978).

[35] A. M. Bradshaw, W. Domcke, and L. S. Cederbaum, Intrinsic and extrinsic plasmon coupling in x-ray photoemission from core states of adsorbed atoms, Phys. Rev. B **16**, 1480 (1977).

[36] J. Fuggle, D. Fabian, and L. Watson, Electron energy loss processes in x-ray photoelectron spectroscopy, J. Electron Spectrosc. Relat. Phenom. **9**, 99 (1976).

[37] W. J. Pardee, G. D. Mahan, D. E. Eastman, R. A. Pollak, L. Ley, F. R. McFeely, S. P. Kowalczyk, and D. A. Shirley, Analysis of surface- and bulk-plasmon contributions to x-ray photoemission spectra, Phys. Rev. B **11**, 3614 (1975).

[38] C. Kalha, N. K. Fernando, P. Bhatt, F. O. L. Johansson, A. Lindblad, H. Rensmo, L. Z. Medina, R. Lindblad, S. Siol, L. P. H. Jeurgens, C. Cancellieri, K. Rossnagel, K. Medjanik, G. Schönhense, M. Simon, A. X. Gray, S. Nemšák, P. Lömker, C. Schlueter, and A. Regoutz, Hard x-ray photoelectron spectroscopy: a snapshot of the state-of-the-art in 2020, J. Phys. Condens. Matter **33**, 233001 (2021).

[39] K. Kobayashi, Hard X-ray photoemission spectroscopy, Nucl. Instrum. Methods Phys. Res., Sect. A **601**, 32 (2009).

[40] C. Fadley, X-ray photoelectron spectroscopy: Progress and perspectives, J. Electron Spectrosc. Relat. Phenom. **178-179**, 2 (2010).

[41] J. C. Woicik, *Hard X-ray Photoelectron Spectroscopy (HAXPES)* (Springer, Cham, 2016), Vol. 59.

[42] A. X. Gray, C. Papp, S. Ueda, B. Balke, Y. Yamashita, L. Plucinski, J. Minár, J. Braun, E. R. Ylvisaker, C. M. Schneider, W. E. Pickett, H. Ebert, K. Kobayashi, and C. S. Fadley, Probing bulk electronic structure with hard x-ray angle-resolved photoemission, Nat. Mater. **10**, 759 (2011).

[43] A. X. Gray, J. Minár, S. Ueda, P. R. Stone, Y. Yamashita, J. Fujii, J. Braun, L. Plucinski, C. M. Schneider, G. Panaccione, H. Ebert, O. D. Dubon, K. Kobayashi, and C. S. Fadley, Bulk electronic structure of the dilute magnetic semiconductor Ga_{1-x} $MnAs_x$ through hard x-ray angle-resolved photoemission, Nat. Mater. **11**, 957 (2012).

[44] J. Nayak, M. Maniraj, A. Rai, S. Singh, P. Rajput, A. Gloskovskii, J. Zegenhagen, D. L. Schlagel, T. A. Lograsso, K. Horn, and S. R. Barman, Bulk electronic structure of quasicrystals, Phys. Rev. Lett. **109**, 216403 (2012).

[45] T. Ohtsuki, A. Chainani, R. Eguchi, M. Matsunami, Y. Takata, M. Taguchi, Y. Nishino, K. Tamasaku, M. Yabashi, T. Ishikawa, M. Oura, Y. Senba, H. Ohashi, and S. Shin, Role of Ti $3d$ carriers in mediating the ferromagnetism of $Co : TiO_2$ anatase thin films, Phys. Rev. Lett. **106**, 047602 (2011).

[46] Y. Takata, Y. Kayanuma, S. Oshima, S. Tanaka, M. Yabashi, K. Tamasaku, Y. Nishino, M. Matsunami, R. Eguchi, A. Chainani, M. Oura, T. Takeuchi, Y. Senba, H. Ohashi, S. Shin, and T. Ishikawa, Recoil effect of photoelectrons in the Fermi edge of simple metals, Phys. Rev. Lett. **101**, 137601 (2008).

[47] M. Sing, G. Berner, K. Goß, A. Müller, A. Ruff, A. Wetscherek, S. Thiel, J. Mannhart, S. A. Pauli, C. W. Schneider, P. R. Willmott, M. Gorgoi, F. Schäfers, and R. Claessen, Profiling the interface electron gas of $LaAlO_3/SrTiO_3$ heterostructures with hard x-ray photoelectron spectroscopy, Phys. Rev. Lett. **102**, 176805 (2009).

[48] S. Sarkar, P. Sadhukhan, V. K. Singh, A. Gloskovskii, K. Deguchi, N. Fujita, and S. R. Barman, Bulk electronic structure of high-order quaternary approximants, Phys. Rev. Res. **3**, 013151 (2021).

[49] S. Sarkar, M. Krajčí, P. Sadhukhan, V. K. Singh, A. Gloskovskii, P. Mandal, V. Fournée, M.-C. de Weerd, J. Ledieu, I. R. Fisher, and S. Roy Barman, Anderson localization of electron states in a quasicrystal, Phys. Rev. B **103**, L241106 (2021).

[50] P. Sadhukhan, S. W. D'Souza, V. K. Singh, R. S. Dhaka, A. Gloskovskii, S. K. Dhar, P. Raychaudhuri, A. Chainani, A. Chakrabarti, and S. Roy Barman, Role of antisite disorder, electron-electron correlations, and a surface valence transition in the electronic structure of $CeMnNi_4$, Phys. Rev. B **99**, 035102 (2019).

[51] P. Sadhukhan, S. Sarkar, S. W. D'Souza, A. Gloskovskii, and S. Roy Barman, Bulk electronic structure of Mn_2NiGa using hard x-ray photoelectron spectroscopy and density functional theory, Phys. Scr. **98**, 055912 (2023).

[52] C. Kunz, B. Cowie, W. Drube, T.-L. Lee, S. Thiess, C. Wild, and J. Zegenhagen, Relative electron inelastic mean free paths for diamond and graphite at 8 keV and intrinsic contributions to the energy-loss, J. Electron Spectrosc. Relat. Phenom. **173**, 29 (2009).

[53] F. Offi, W. S. M. Werner, M. Sacchi, P. Torelli, M. Cautero, G. Cautero, A. Fondacaro, S. Huotari, G. Monaco, G. Paolicelli, W. Smekal, G. Stefani, and G. Panaccione, Comparison of hard and soft x-ray photoelectron spectra of silicon, Phys. Rev. B **76**, 085422 (2007).

[54] M. Novák, S. Egri, L. Kövér, I. Cserny, W. Drube, and W. Werner, Energy dependence of electron energy loss processes in Ge 2s photoemission, Surf. Sci. **601**, 2344 (2007).

[55] D. G. David, C. Godet, F. O. Johansson, and A. Lindblad, Quantitative analysis of plasmon excitations in hard x-ray photoelectron spectra of bulk black phosphorus, Appl. Surf. Sci. **505**, 144385 (2020).

[56] T. Konishi, S. Ueda, and T. Kinoshita, Quantitative analysis of energy loss processes for the core level intensities in hard x-ray photoemission, J. Electron Spectrosc. Relat. Phenom. **264**, 147314 (2023).

[57] J.-J. Chang and D. C. Langreth, Deep-hole excitations in solids. II. plasmons and surface effects in x-ray photoemission, Phys. Rev. B **8**, 4638 (1973).

[58] C. Schlueter, A. Gloskovskii, K. Ederer, I. Schostak, S. Piec, I. Sarkar, Y. Matveyev, P. Lömker, M. Sing, R. Claessen, C. Wiemann, C. M. Schneider, K. Medjanik, G. Schönhense, P. Amann, A. Nilsson, and W. Drube, The new dedicated HAXPES beamline P22 at PETRAIII, in *AIP Conference Proceedings* (AIP, Melville, NY, 2019), Vol. 2054, p. 040010.

[59] S. Doniach and M. Sunjic, Many-electron singularity in X-ray photoemission and X-ray line spectra from metals, J. Phys. C: Solid State Phys. **3**, 285 (1970).

[60] See Supplemental Material at http://link.aps.org/supplemental/10.1103/PhysRevB.109.205419 for the theoretical plasmon line shapes from the literature [3], HAXPES Al survey spectrum, completely oxidized Al spectra in normal and grazing emission, comparison of Al VB for sputtered and scraped surface, Al PDOS from literature [79] and the VB calculated with it, and the calculation of the Mg XPS VB and the Mg plasmon intensities from XPS experiment [34] and theory [14]. The Supplemental Material contains Figs. S1– S6.

[61] $\frac{I_o}{1+[(E_K-E_K^p)/\Gamma(E)]^2}$, where the half-width at half-maximum $\Gamma(E) = \Gamma_R$ when $E_K > E_K^p$ (E_K^p is the peak position in the kinetic energy scale, E_K) and $\Gamma(E) = \Gamma_L$ when $E_K < E_K^p$, and I_o is the intensity.

[62] S. Tougaard, Practical algorithm for background subtraction, Surf. Sci. **216**, 343 (1989).

[63] C. Jansson, H. Hansen, F. Yubero, and S. Tougaard, Accuracy of the Tougaard method for quantitative surface analysis. Comparison of the Universal and REELS inelastic cross sections, J. Electron Spectrosc. Relat. Phenom. **60**, 301 (1992).

[64] P. Sadhukhan, S. Barman, T. Roy, V. K. Singh, S. Sarkar, A. Chakrabarti, and S. R. Barman, Electronic structure of Au-Sn compounds grown on Au(111), Phys. Rev. B **100**, 235404 (2019).

[65] P. Blaha, K. Schwarz, G. Madsen, D. Kvasnicka, and J. Luitz, User's Guide, WIEN2K, An Augmented Plane Wave Plus Local Orbitals Program for Calculating Crystal Properties.

[66] J. P. Perdew, K. Burke, and M. Ernzerhof, Generalized Gradient Approximation made simple, Phys. Rev. Lett. **77**, 3865 (1996).

[67] M. B. Trzhaskovskaya and V. G. Yarzhemsky, Dirac–Fock photoionization parameters for HAXPES applications, At. Data Nucl. Data Tables **119**, 99 (2018).

[68] P. Sadhukhan, Electronic structure and morphology of manganese based alloys and thin films, Ph.D. thesis, Devi Ahilya Vishwavidyalaya, UGC-DAE Consortium for Scientific Research, Indore (2021), available at http://hdl.handle.net/10603/393275.

[69] A. Fujimori and F. Minami, Valence-band photoemission and optical absorption in nickel compounds, Phys. Rev. B **30**, 957 (1984).

[70] S. R. Barman and D. D. Sarma, Electronic structures of gallium and indium across the solid-liquid transition, Phys. Rev. B **51**, 4007 (1995).

[71] C. Biswas, A. K. Shukla, S. Banik, S. R. Barman, and A. Chakrabarti, Argon nanobubbles in Al(111): A photoemission study, Phys. Rev. Lett. **92**, 115506 (2004).

[72] R. S. Dhaka, C. Biswas, A. K. Shukla, S. R. Barman, and A. Chakrabarti, Xe and Ar nanobubbles in Al studied by photoemission spectroscopy, Phys. Rev. B **77**, 104119 (2008).

[73] R. S. Dhaka and S. R. Barman, Plasmon excitations by photoelectron emission from rare gas nanobubbles in Aluminum, Phys. Rev. Lett. **104**, 036803 (2010).

[74] $P_{int}(n)$, the probability of intrinsic process for the nth plasmon is given by $e^{-\beta} \frac{\beta^n}{n!}$.

[75] $\chi = \alpha^n e^{-\beta} \beta^n / n!$.

[76] S. Tanuma, C. J. Powell, and D. R. Penn, Calculations of electron inelastic mean free paths. IX. data for 41 elemental solids over the 50 eV to 30 keV range, Surf. Interface Anal. **43**, 689 (2011).

[77] B. R. Strohmeier, An ESCA method for determining the oxide thickness on Aluminum alloys, Surf. Interface Anal. **15**, 51 (1990).

[78] J. Bhattacharya, P. Sadhukhan, S. Sarkar, V. K. Singh, A. Gloskovskii, S. R. Barman, and A. Chakrabarti, Bulk electronic structure of Ni_2MnGa studied by density functional theory and hard x-ray photoelectron spectroscopy, Phys. Rev. B **108**, L121114 (2023).

[79] P. Leonard, Energy bands, densities of states and x-ray spectra of Al with superposed self-consistent potentials, J. Phys. F: Met. Phys. **8**, 467 (1978).

[80] R. P. Gupta and A. J. Freeman, Band-structure contributions to x-ray emission and absorption spectra and edges in magnesium, Phys. Rev. Lett. **36**, 1194 (1976).

[81] D. C. Langreth, Singularities in the x-ray spectra of metals, Phys. Rev. B **1**, 471 (1970).

[82] V. K. Singh, M. Krajčí, S. Sarkar, M. Balal, S. Barman, P. Sadhukhan, A. Gloskovskii, M. Feuerbacher, C. Thomas, P. Ebert, E. Rotenberg, K. Horn, and S. Roy Barman, Electronic structure of $\beta - Al_3Mg_2$ and $Al_{13}Fe_4$ complex metallic alloys, Phys. Rev. B **105**, 205107 (2022).